PERGAMON

International Journal of Solids and Structures 39 (2002) 5615–5632

INTERNATIONAL JOURNAL OF SOLIDS and STRUCTURES

www.elsevier.com/locate/ijsolstr

The dynamics of multiple neck formation and fragmentation in high rate extension of ductile materials

P.R. Guduru, L.B. Freund *

Division of Engineering, Brown University, Box D, 182 Hope Street, Providence, RI 02912-9104, USA

Received 4 October 2001; received in revised form 8 February 2002

Abstract

Dynamic necking bifurcation in rapidly extending cylindrical rods is investigated. It has been found that both short wavelength and long wavelength perturbations are suppressed by inertia and an intermediate wavelength is favored. The analysis predicts an increase in the number of necks and an increase in the bifurcation strain with increasing extension rate, in agreement with experimental observations. In terms of the number of necks formed as a function of extension rate, good agreement has been found between the experiments and the analysis. At any given aspect ratio, the model also predicts that beyond a critical extension rate, the mode number of the dominant perturbation increases rapidly and the perturbation begins to look more like a surface instability. This could lead to a fragmentation mechanism at high extension speeds which is different from multiple necking. Currently no experimental results are available to test this prediction. Numerical simulations have been conducted to simulate the fragmentation results, using Gurson's constitutive law along with a porous failure criterion. Good agreement between the experimental observations and the numerical results has been obtained for the fragmentation statistics. However, the numerical results consistently overestimate the number of necks and the fracture strain, possibly due to uncertainty in the constitutive data used, especially at large strains.

Keywords: Ductile fragmentation; Dynamics; Stability and bifurcation; Porous plasticity; Multiple necking

1. Introduction

Grady and Benson (1983) conducted fragmentation studies on rapidly expanding ductile metal rings by subjecting them to radial electromagnetic loading. The rings were made of either 1100-O aluminum or OFHC copper. They observed multiple necking along the circumference of the ring. Some of these necks arrested before fracture and the others led to fracture, resulting in a number of fragments. They repeated these experiments at a variety of loading rates and observed the following trends. (i) The number of fragments is an increasing function of the expansion speed. (ii) The fracture strain is an increasing function of the expansion speed. This can be interpreted as increased ductility at higher loading rates. Altynova et al.

---

* Corresponding author. Tel.: +1-401-863-1476; fax: +1-401-863-1157/2857.
E-mail address: freund@engin.brown.edu (L.B. Freund).

PII: S0020-7683(02)00367-0

(1996) performed similar experiments and observed the same fragmentation behavior. They also performed a one dimensional rigid-viscoplastic dynamic finite element analysis and suggested that the inertial effects are responsible for the increased ductility at higher loading rates. Fyfe and Rajendran (1980) subjected thin cylindrical specimens to radial loading and observed similar trends.

A number of analytical efforts have been made to model the increased ductility and the tendency to form more fragments at higher loading rates. These models attempted to quantify the effect of inertia on necking instabilities in uniformly deforming straight rods. The necking instability in rods under quasi-static uniaxial loading has been studied by Miles (1971), Cheng et al. (1971), Hutchinson and Miles (1974) and Hill and Hutchinson (1975). The general approach has been to use perturbation analysis in order to determine the critical stress state at which a non-homogeneous, neck-like deformation field can exist. Hutchinson and Miles (1974) showed that such a deformation field can exist at a critical stress, which is greater than the stress at maximum load, and the lowest critical stress corresponds to the longest wavelength perturbation, in other words, a single neck is formed at this critical stress. Shenoy and Freund (1999) generalized the perturbation analysis of Hill and Hutchinson (1975) to study a rectangular block of material, dynamically loaded in plane strain, using a hypoelastic constitutive relation. They examined the growth rate of neck-like perturbations and found that short as well as long wavelength perturbations are suppressed and intermediate wavelengths have the highest rate of growth. Their analysis captured the qualitative features of the experimental observations such as the increasing number of necks and the increasing ductility with an increase in extension rate. However, direct comparison with experiments could not be performed, as it was a plane strain analysis.

In this paper, the perturbation analysis of Shenoy and Freund (1999) is adapted to an extending cylinder in order to facilitate direct comparison with the experiments of Grady and Benson (1983). This work is a generalization of the analysis of Hutchinson and Miles (1974) to include inertial effects. In earlier work, Fyfe and Rajendran (1980) extended the analysis of Hutchinson and Neale (1977) to demonstrate the effect of strain rate on ductility. Fressengeas and Molinari (1994) used a viscoplastic constitutive relation and concluded that inertia suppresses long wavelength necking whereas viscosity diminishes short wavelength necking patters. However, as demonstrated by Shenoy and Freund (1999), inertia alone can be shown to suppress the growth of both short and long wavelength modes.

Numerical modeling of expanding rings was performed by Han and Tvergaard (1995), Pandolfi et al. (1999) and most recently by Sorensen and Freund (2000). Sorensen and Freund (2000) conducted a plane strain numerical investigation of the formation of multiple necks in a radially expanding ring and found that long wavelength thickness imperfections lead to the appearance of a nearly periodic short wavelength necking pattern. Plastic strain rate sensitivity was shown to have only a minor influence on the early stages of development of unstable necking. In the current investigation, the expanding rings used by Grady and Benson (1983) in their experiments are modeled as homogeneously deforming cylindrical rods, with a constitutive law that includes ductile void growth. Statistics of numerical fragmentation simulations are compared with those observed in the experiments.

The next two sections describe the homogeneous deformation of an expanding ring and a perturbation analysis of such a deformation, respectively. Following a discussion of the results of the perturbation analysis, a numerical study of the same problem is presented along with a comparison with the experimental observations.

2. Homogeneous deformation of a cylindrical bar

In the following analysis, the expanding ring of the Grady and Benson (1983) experiment is idealized to be a homogeneously deforming incompressible cylindrical bar of initial radius A and initial length $2L$, as shown in Fig. 1. The radius A is chosen such that the cross sectional area of the cylinder is equal to that of

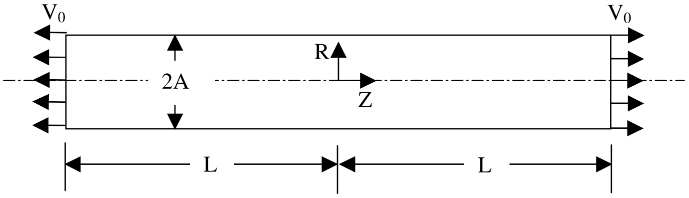

Fig. 1. Geometry of the extending cylinder.

the rings used in the experiments, which had square cross sections. The ends of the rod move in opposite directions with a speed v_0 as shown. Denoting the reference coordinates of mass particles as (R, Θ, Z) and current coordinates as (r, θ, z), the deformation can be described as

$$r = \lambda^{-1/2}R, \quad z = \lambda Z \quad \text{and} \quad \theta = \Theta \tag{1}$$

where

$$\lambda = 1 + v_0 t/L \tag{2}$$

with t representing time. Using Eqs. (1) and (2), the velocity field corresponding to the homogeneous deformation state is

$$v_r = -\frac{v_0}{2L}R\left(1 + \frac{v_0}{L}t\right)^{-3/2} \quad \text{and} \quad v_z = \frac{v_0}{L}Z \tag{3}$$

The fields $v_r(R, Z, t)$ and $v_z(R, Z, t)$ are the radial and axial components of the velocity. The Cauchy stress $\boldsymbol{\sigma}$ for this homogeneous deformation is

$$\boldsymbol{\sigma} = \begin{bmatrix} 0 & 0 & 0 \\ 0 & 0 & 0 \\ 0 & 0 & \sigma \end{bmatrix} + \begin{bmatrix} -p & 0 & 0 \\ 0 & -p & 0 \\ 0 & 0 & -p \end{bmatrix} \tag{4}$$

where σ is the axial stress due to strain history and p is the hydrostatic stress due to particle acceleration (see Eq. (3)). Using the equation of motion in the radial direction and the condition that $p = 0$ at $R = A$, p can be determined to be

$$p = \frac{3}{8}\rho\left(\frac{v_0}{L}\right)^2 \frac{(A^2 - R^2)}{(1 + v_0 t/L)^3} \tag{5}$$

A similar expression has been derived for the plane strain case by Shenoy and Freund (1999), where the denominator had a power 4 instead of 3 and a numerical factor of 1 instead of 3/8. In the above equation, ρ is the mass density. Eq. (3) describes the deformation state and σ is not known because no constitutive relation has been used yet. The stability of this deformation state is analyzed next. In other words, if the velocity field given by Eq. (3) is slightly perturbed in a way that is consistent with the boundary conditions, we examine if such a perturbation grows in time and, if it does, what is its rate of growth.

3. Linear perturbation analysis

The equations of motion in rate form in terms of the components of the first Piola–Kirchoff stress $\boldsymbol{T}$ are

$$\dot{T}_{Rr,R} + \dot{T}_{Zr,Z} + (\dot{T}_{Rr} - \dot{T}_{\Theta\theta})/R = \rho\ddot{v}_r \tag{6}$$

$$\dot{T}_{Rz,R} + \dot{T}_{Zz,Z} + \dot{T}_{Rz}/R = \rho\ddot{v}_z \tag{7}$$

All derivatives with respect to Θ are set to zero in writing these equations due to axial symmetry. The boundary conditions are

$$v_z(R, \pm L, t) = \pm v_0 \tag{8}$$

$$\dot{T}_{Rz}(A, Z, t) = 0, \qquad \dot{T}_{Rr}(A, Z, t) = 0, \qquad \dot{T}_{Zr}(R, \pm L, t) = 0 \tag{9}$$

which ensure constant mean strain rate, traction free lateral faces and shear stress free ends. In the above equations, $\dot{\boldsymbol{T}}$ can be expressed in terms of Cauchy stress and deformation quantities using

$$\dot{\boldsymbol{T}} = \boldsymbol{F}^{-1}(\hat{\boldsymbol{\sigma}} - \boldsymbol{D}\boldsymbol{\sigma} - \boldsymbol{W}) \tag{10}$$

where $\boldsymbol{F}$ is the deformation gradient, $\hat{\boldsymbol{\sigma}}$ is the Jaumann rate of Cauchy stress, and $\boldsymbol{D}$ and $\boldsymbol{W}$ are the symmetric and antisymmetric parts of velocity gradient. The material is assumed to follow the hypoelastic constitutive relation developed by Storen and Rice (1975), which in the present context becomes

$$\hat{\sigma}'_{rr} = (h + h_1)D_{rr} + (h - h_1)D_{\theta\theta} \tag{11}$$

$$\hat{\sigma}'_{\theta\theta} = (h - h_1)D_{rr} + (h + h_1)D_{\theta\theta} \tag{12}$$

$$\hat{\sigma}'_{zz} = 2hD_{zz} \tag{13}$$

$$\hat{\sigma}'_{rz} = 2h_1D_{rz} \tag{14}$$

where prime denotes the deviatoric component. In writing Eqs. (11)–(14), it was assumed that $v_\theta = 0$, all derivatives with respect to θ are zero and $D_{rr} + D_{\theta\theta} + D_{zz} = 0$. Here h and h_1 are, respectively, the tangent modulus and the secant modulus of the graph of equivalent stress $\sqrt{\sigma'_{ij}\sigma'_{ij}/2}$ vs. equivalent strain $\sqrt{2\varepsilon_{ij}\varepsilon_{ij}}$. This graph reduces to the shear stress vs. shear strain curve in pure shear. It can be verified that the homogeneous solution given by Eqs. (3)–(5) satisfies Eqs. (6)–(14). In addition, σ at any time can be calculated by integrating Eqs. (11)–(14).

Introduce, at some time τ, a perturbation velocity field (v'_r, v'_θ, v'_z) such that $v'_\theta = 0$ and v'_r and v'_z do not depend on θ. Then, it can be seen that this perturbation velocity field, along with the corresponding perturbation stress field satisfies Eqs. (6)–(14), with Eq. (8) modified as

$$v'_z(R \pm L, t) = 0 \tag{15}$$

Dropping the prime for convenience, Eqs. (6) and (7) and Eqs. (9)–(15) are the governing equations for the perturbation velocity field. The task is now reduced to analyzing the evolution of this field. Without loss of generality, τ can be set to zero so that $\boldsymbol{F} = \boldsymbol{1}$. The reference and current configurations coincide with each other and the distinction between (R, Θ, Z) and (r, θ, z) can be neglected. Note that Eqs. (11)–(14) do not determine the hydrostatic component of the stress rate. In order to eliminate it, Eq. (6) is differentiated with respect to z and Eq. (7) with respect to r and the difference between them is formed. This results in

$$(\dot{T}_{rr} - \dot{T}_{zz})_{,zr} + \dot{T}_{zr,zz} + (\dot{T}_{rr} - \dot{T}_{\theta\theta})_{,z}/r - \dot{T}_{rz,rr} - \dot{T}_{rz,r}/r + \dot{T}_{rz}/r^2 = \rho(\ddot{v}_{r,z} - \ddot{v}_{z,r}) \tag{16}$$

Using Eqs. (10)–(14) in the above equation gives

$$\begin{aligned} &(h + \sigma/2)v_{r,rrz} + [-p_{,r} + (h + \sigma/2)/r)]v_{r,rz} - \left[p_{,rr} + p_{,r}/r + (h + \sigma/2)/r^2\right]v_{r,z} + (h_1 - 2h + \sigma/2)v_{z,rzz} \\ &\quad - p_{,r}v_{z,zz} + (h_1 + \sigma/2)v_{r,zzz} - (h_1 - \sigma/2)v_{z,rrr} - \frac{1}{r}(h_1 - \sigma/2)v_{z,rr} + \frac{1}{r^2}(h_1 - \sigma/2)v_{z,r} = \rho\left(\ddot{v}_{r,z} - \ddot{v}_{z,r}\right) \end{aligned} \tag{17}$$

Since the material is incompressible, v_r and v_z can be written in terms of a potential $\varphi(r,z,t)$ as $v_r = -\varphi_{,z}$ and $v_z = \frac{1}{r}(r\varphi)_{,r}$. Defining $\alpha = (3/4)\rho(v_0/L)^2$, Eq. (17) becomes

$$\begin{aligned}
&\frac{1}{2}(\sigma - 2h_1)\varphi_{,rrrr} - \frac{1}{2}(\sigma + 2h_1)\varphi_{,zzzz} - (3h - h_1)\varphi_{,rrzz} + \frac{1}{r}(\sigma - 2h_1)\varphi_{,rrr} - \frac{1}{r}(3h - h_1)\varphi_{,rzz} \\
&\quad - \frac{3}{2r^2}(\sigma - 2h_1)\varphi_{,rr} + \left(\frac{3h - h_1}{r^2} - \alpha\right)\varphi_{,zz} + \frac{3}{2r^3}(\sigma - 2h_1)\varphi_{,r} \\
&\quad - \frac{3}{2r^4}(\sigma - 2h_1)\varphi = \rho\left(-\ddot{\varphi}_{,rr} - \ddot{\varphi}_{,zz} - \frac{\ddot{\varphi}_{,r}}{r} + \frac{\ddot{\varphi}}{r^2}\right) \qquad (18)
\end{aligned}$$

Assuming a separable solution of the form

$$\varphi(r,z,t) = \psi(r,z)T(t) \qquad (19)$$

results in an equation for $\psi(r,z)$ as

$$\begin{aligned}
&\frac{1}{2}(\sigma - 2h_1)\psi_{,rrrr} - \frac{1}{2}(\sigma + 2h_1)\psi_{,zzzz} - (3h - h_1)\psi_{,rrzz} + \frac{1}{r}(\sigma - 2h_1)\psi_{,rrr} - \frac{1}{r}(3h - h_1)\psi_{,rzz} \\
&\quad + \left[\rho\theta^2 - \frac{3}{2r^2}(\sigma - 2h_1)\right]\psi_{,rr} + \left(\frac{3h - h_1}{r^2} + \rho\theta^2 - \alpha\right)\psi_{,zz} + \left[\frac{3}{2r^3}(\sigma - 2h_1) + \rho\theta^2/r\right]\psi_{,r} \\
&\quad - \left[\frac{3}{2r^4}(\sigma - 2h_1) + \rho\theta^2/r^2\right]\psi = 0 \qquad (20)
\end{aligned}$$

where $\theta^2 = \frac{\ddot{T}}{T}$ is the separation constant. If θ^2 is real and positive, the perturbation field is unstable. The function ψ is assumed to have the form

$$\psi(r,z) = g(r)\cos(\gamma z) \qquad (21)$$

where γ is the axial wave number of the perturbation field. In order to satisfy the boundary condition Eq. (15), γ must have the values

$$\gamma = \frac{\pi q}{2L}, \quad q = 1, 3, 5, \ldots \qquad (22)$$

Using Eq. (21) in Eq. (20), the governing equation for $g(r)$ is obtained as

$$\begin{aligned}
&g'''' + \frac{2}{r}g''' + \left[\frac{\gamma^2(3h - h_1) + \rho\theta^2}{\sigma/2 - h_1} - \frac{3}{r^2}\right]g'' + \left[\frac{\gamma^2(3h - h_1) + \rho\theta^2}{r(\sigma/2 - h_1)} + \frac{3}{r^3}\right]g' \\
&\quad - \left[\frac{\gamma^2(3h - h_1) + \rho\theta^2}{r^2(\sigma/2 - h_1)} + \frac{3}{r^4} + \frac{\gamma^2(\rho\theta^2 - \alpha) + \gamma^4(\sigma/2 + h_1)}{\sigma/2 - h_1}\right]g = 0 \qquad (23)
\end{aligned}$$

Assume a power law type uniaxial stress–strain relation, $\sigma = k\varepsilon^n$, where k and n are material constants with n denoting the strain hardening exponent. With such a relation, $n = h/h_1$. By defining

$$\begin{aligned}
b &= [3 - 1/n + 12N(v_0/v_p)^2/(\pi^2 q^2 n(ns)^{n-1})]/(3s - 2/n) \\
c &= [(1/n + 3s/2) + 3(4N - 3)(v_0/v_p)^2/(\pi^2 q^2 n(ns)^{n-1})]/(1/n - 3s/2)
\end{aligned}$$

in which $s = \sigma/3h$, $v_p = \sqrt{k/\rho}$ and $N = (L\theta/v_0)^2$, one can write Eq. (23) as

$$\boldsymbol{L}^2(g) + 2b\gamma^2\boldsymbol{L}(g) + c\gamma^4 g = 0 \qquad (24)$$

where the operator $\boldsymbol{L}$ is defined by $\boldsymbol{L}(g) = g'' + g'/r - g/r^2$. Further, by setting $\rho_1^2 = b - \sqrt{b^2 - c}$ and $\rho_1^2 = b + \sqrt{b^2 - c}$, we can represent Eq. (24) as

$$\left(\boldsymbol{L}+\gamma^2\rho_1^2\right)\left(\boldsymbol{L}+\gamma^2\rho_2^2\right)g=0 \tag{25}$$

The boundary conditions, Eq. (9), give

$$g''(A)+\frac{1}{A}g'(A+\left(\gamma^2-1/A^2\right)g(A)=0 \tag{26}$$

$$g'''(A)+\frac{2}{A}g''(A)+\left(2b\gamma^2-1/A^2\right)g'(A)+\left[\frac{1}{A^3}+\frac{2\gamma^2}{A}\left(b-\frac{h_1}{\sigma/2-h_1}\right)+\frac{\gamma^2\alpha A}{\sigma/2-h_1}\right]g(A)=0 \tag{27}$$

Eq. (26) is obtained from the first of the Eq. (9). Eq. (27) is obtained by setting $\dot{T}_{Rr,Z}(A,Z,t)=0$. An expression for $\dot{T}_{Rr,Z}$ is obtained using Eqs. (10) and (7). Non-trivial solutions of Eq. (25) are sought subject to constraints Eqs. (26) and (27). The solution to Eq. (25) has different forms depending on the complex character of ρ_1^2 and ρ_2^2. The relevant case here is the one when ρ_1^2 and ρ_2^2 form a complex conjugate pair, in which case Eq. (25) admits a solution of the form

$$g(r)=BJ_1(\gamma\rho r)+\overline{B}J_1(\gamma\bar{\rho}r) \tag{28}$$

where the bar denotes complex conjugate. B is an arbitrary complex constant and ρ is a square root of either ρ_1^2 or ρ_2^2. J_n is the Bessel function of order n. Subject to Eqs. (26) and (27), the condition for the existence of a non-trivial B is

$$\mathrm{Im}\{(1-\bar{\rho}^2)J_1(\gamma\bar{\rho}A)\lfloor(C_1-C_2)J_1(\gamma\rho A)+\gamma\rho A(C_3-\rho^2)J_0(\gamma\rho A)\rfloor]\}=0 \tag{29}$$

where Im stands for the imaginary part and

$$C_1=\frac{\frac{9}{4}(A/L)^2\left(v_0/v_p\right)^2}{n(ns)^{n-1}(3s/2-1/n)},\quad C_2=\frac{2}{(3ns/2-1)}$$

$$C_3=\frac{3(1-s/2)}{(3s/2-1/n)}+\frac{12N\left(v_0/v_p\right)^2}{\pi^2q^2n(ns)^{n-1}(3s/2-1/n)}$$

In the above equations, $N=(L\theta/v_0)^2$ can interpreted as the rate of growth of the perturbation relative to the background homogeneous rate of stretch. N is required to be very large compared to 1 for a perturbation mode q to result in multiple necking. For a given strain hardening exponent n, stress s, aspect ratio A/L, extension speed v_0/v_p and perturbation mode q, Eq. (29) determines the rate of growth N.

4. Results of perturbation analysis

The calculation procedure is described first. For a given hardening exponent n, aspect ratio $\beta=A/L$, stress s and extension rate v_0/v_p, Eq. (29) is solved for the growth rate N as a function of the perturbation mode q. As q is increased, initially N also increases, reaches a maximum and then begins to decrease. The value of q corresponding to the maximum value of N, say $N_{\max}$, is termed $q_{\max}$ and it represents the dominant perturbation mode for the given value of s. However, we require $N_{\max}\gg 1$ for the perturbation mode $q_{\max}$ to turn in to a necking mode. Hence, a given mode $q_{\max}$ is supposed to satisfy a failure criterion when $N_{\max}=N_{\mathrm{C}}$, where N_{C} is an arbitrarily chosen large number. In the following analysis, N_{C} is chosen to be 200. If $N_{\max}<N_{\mathrm{C}}$, s is increased gradually until $N_{\max}=N_{\mathrm{C}}$. The corresponding s is the critical stress s_{c} for necking bifurcation. A plot of the perturbation growth rate N as a function of q is shown in Fig. 2 for $N_{\mathrm{C}}=200$ and for different values of the normalized loading rate v_0/v_p. The corresponding values of critical stress s_{c} are also shown. This plot gives the number m of unstable necks at a given loading rate, as predicted by the above analysis, to be $m=(q_{\max}-1)/2$. It also gives the critical stress s_{c} at which multiple necking

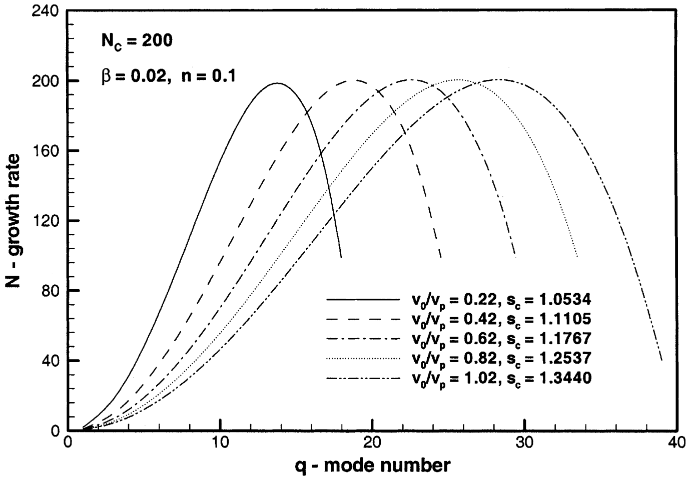

Fig. 2. Perturbation growth rate as a function of its mode number. Inertia suppresses the growth of low as well as high perturbation modes and promotes intermediate modes.

begins. The fragmentation experiments of Grady and Benson (1983) and Altynova et al. (1996) showed that the number of necks/fragments increases with an increase in extension rate and the fracture strain increases with an increase in extension rate. The current analysis quantifies these observations, as illustrated in Fig. 3 and Fig. 4. Fig. 3 shows the number of necks as a function of extension rate, for different hardening exponents. The analysis predicts that the hardening exponent has little effect on the number of necks, within the range of v_0/v_p plotted in Fig. 3. Fig. 4 shows an almost linear increase in critical strain, which is again independent of the hardening exponent. One of the drawbacks of the analysis presented above is the arbitrary choice of N_C. However, the number of necks is weakly dependent on N_C. An increase in N_C from 100 to 2000 results in an increase in the number of necks by a factor of 2–3, which was also a result obtained by Shenoy and Freund (1999) for plane strain extension. Thus, a judicious choice of N_C could possibly be made

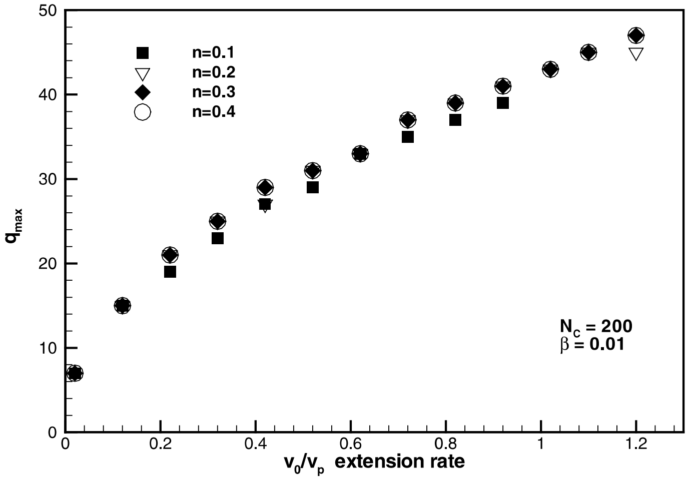

Fig. 3. Effect of extension speed on the dominant perturbation mode. Higher perturbation implies more necks. Strain hardening has no significant effect on the dominant mode.

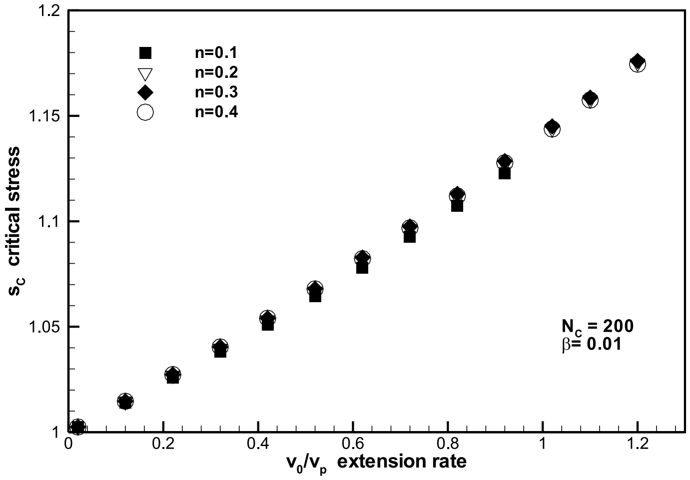

Fig. 4. Effect of extension rate on the bifurcation stress or bifurcation strain ($s = \varepsilon/n$). This figure explains the experimentally observed increase in the ductility of metal rings at higher extension speeds. Strain hardening has so significant role.

from an appropriate comparison with experiments. The effect of decreasing the aspect ratio at a given extension speed is to increase the necking mode number and to decrease the critical stress.

The functional relation between the necking mode, the aspect ratio, the critical growth rate and the extension speed can be summarized through a universal relation shown in Fig. 5. If we fix the value of N_C, the necking mode for all values of the aspect ratio, within the extension speed range shown, can be obtained from a single curve in Fig. 5 which can be represented as

$$q_{\max} = N_C^{1/4}\beta^{-1/2}\left(\frac{v_0}{v_p}\right)^{1/2} \tag{30}$$

Comparison of the perturbation analysis results with the experimental observations requires information about the constitutive behavior of the material at the high strain rates. A typical strain rate in the ex-

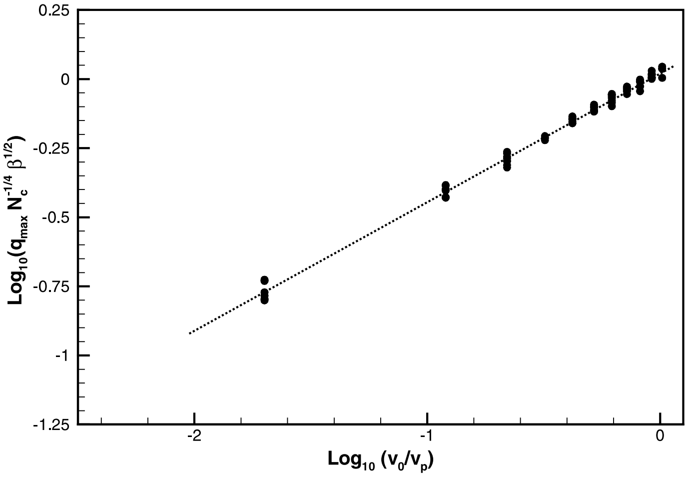

Fig. 5. A universal law relates the dominant perturbation mode, N_C, aspect ratio and the extension speed. By choosing an appropriate value for N_C, necking mode for all speeds and aspect ratios can be obtained from a single curve shown here.

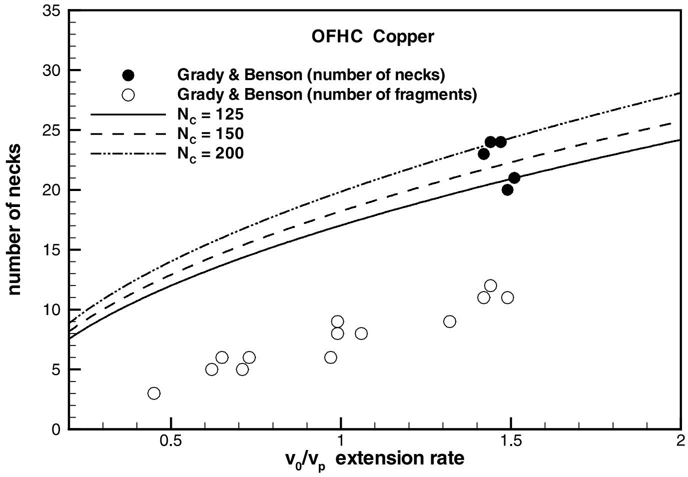

Fig. 6. Comparison between the model predictions and the experiment for three values of N_C for copper.

periments of Grady and Benson (1983) on aluminum and copper rings was around 10^4/s. For these materials, this is also the strain rate around which there is a sharp increase in the flow stress. Thus, the accuracy of the constitutive data available places a limitation on the comparison with the experimental results. The aspect ratio β in these experiments is 0.0113. Fig. 6 compares the number of necks observed in the fragmentation experiments of Grady and Benson (1983) on OFHC copper rings with the analysis predictions, for three different choices of N_C. Constitutive parameters used are $k = 760$ MPa and $n = 0.49$, which were obtained by fitting the power law to the stress–strain data reported by Follansbee (1986) at a strain rate of 1.2×10^4/s. A value of 125–200 for N_C appears to fit the experiments well. Similar comparison for 1100-O aluminum is shown in Fig. 7. Constitutive parameters used are $k = 230$ MPa and $n = 0.33$, which were obtained from the data reported by Pao and Gilat (1989) at a strain rate of 10^3/s. A choice of

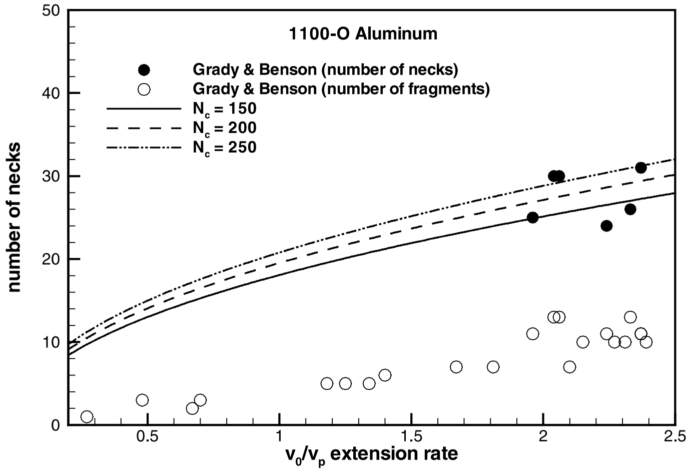

Fig. 7. Comparison between the model predictions and the experiment for three values of N_C for aluminum. For both copper and aluminum, the values of N_C for which good agreement was found, are approximately the same. This gives a predictive capability to the perturbation analysis.

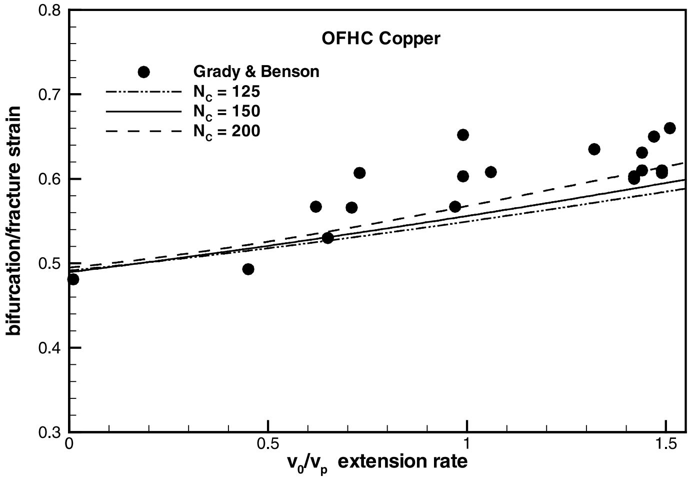

Fig. 8. A comparison of the bifurcation strain as predicted by the model with the experimentally observed fracture strain for copper.

150–250 for N_C appears to yield good agreement with the experimental results. It is significant that for two different materials, tested at very different extension speeds, the value of N_C that makes the analysis predictions and the experimental observations agree is almost the same. This gives the above perturbation analysis a predictive capability. By choosing N_C to be 200 and given the aspect ratio, the universal relation shown in Fig. 5 can predict the number of necks for any material, if the stress–strain relation for that material is known. Further experimental results are awaited to test the validity of such predictions.

Figs. 8 and 9 show the comparison between the bifurcation strain from the analysis and the fracture strain measured by Grady and Benson (1983) for copper and aluminum respectively, for three values of N_C. Fracture strain, defined as the change in the total length of all fragments with respect to the initial ring length, must overestimate the bifurcation strain. This is indeed the case for copper whereas the bifurcation strain is slightly higher than fracture strain for aluminum. Such a discrepancy can be attributed to the uncertainty in the constitutive data used in the analysis. However, it is noteworthy that the increase in the bifurcation strain and the fracture strain are very similar to each other.

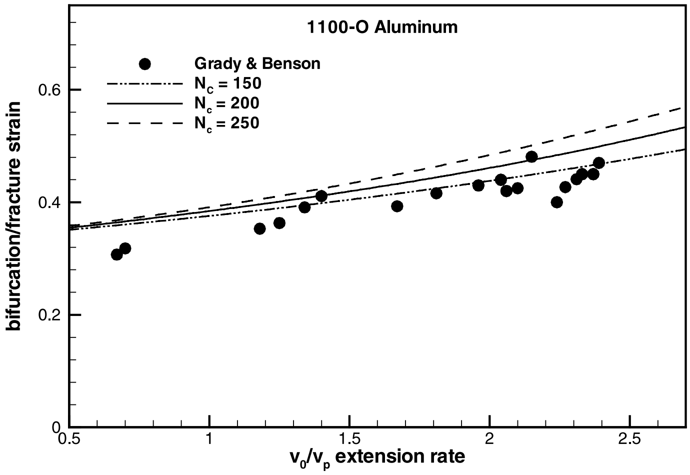

Fig. 9. A comparison of the bifurcation strain as predicted by the model with the experimentally observed fracture strain for aluminum.

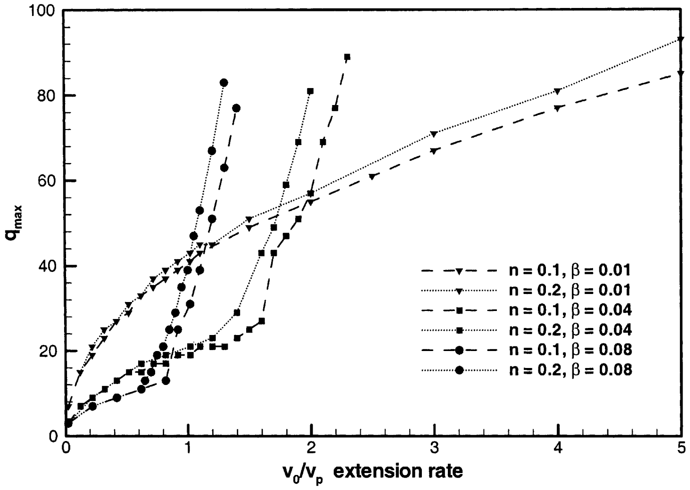

Fig. 10. A dramatic increase in the dominant perturbation is observed beyond a critical extension rate, which is a strong function of the aspect ratio and a weak function of hardening exponent.

A dramatically different behavior was observed for the number of necks and the bifurcation strain when the extension speed v_0 is increased to values significantly higher than those in the experiments. Fig. 10 shows the variation of the dominant perturbation mode number over a larger range of extension rate, for three aspect ratios and two values of the hardening exponent. It can be seen that the earlier discussion on the effect of aspect ratio and the hardening exponent on the mode number is valid for the normalized extension rate below 1. The mode number is seen to increase rapidly beyond a critical extension speed and this critical speed decreases as the aspect ratio increases, that is, as the bar becomes less slender. As the number of necks increases rapidly, the stress is seen to saturate at the same value for all aspect ratios and this level is found to be a decreasing function of the hardening exponent, as shown in Fig. 11. In order to understand this

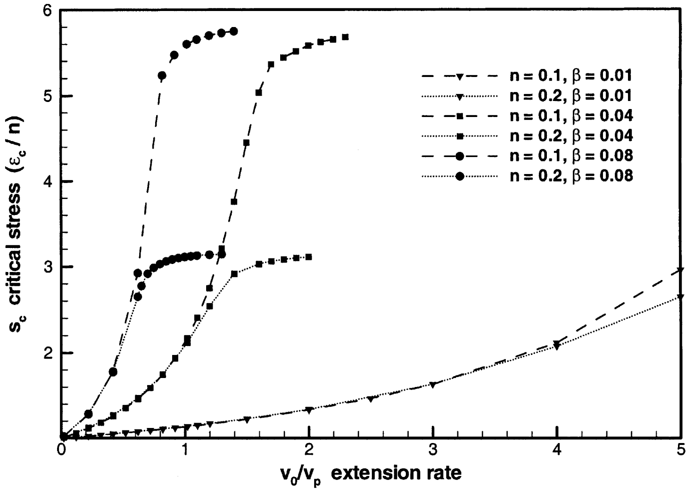

Fig. 11. At higher extension rates, critical stress corresponding to the dominant mode reaches a saturation value which is a strong function of the hardening exponent and does not depend on the aspect ratio.

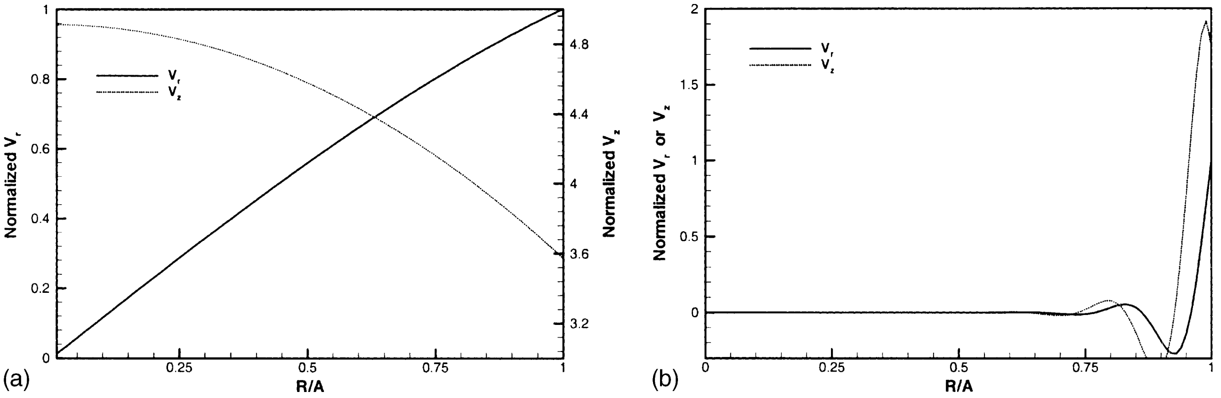

Fig. 12. Transition of neck like perturbations into surface instabilities at high extension speeds. (a) Normalized radial and axial perturbation velocities that represent necking deformation at $v_0/v_p = 0.2$. (b) The perturbation velocity components are localized to near the surface at $v_0/v_p = 5$. This looks more like a surface perturbation than a necking mode.

behavior, it is instructive to examine the radial and axial velocity distribution corresponding to the dominant perturbation. At low values of v_0, Fig. 12a shows the variation of the amplitude of the radial and axial velocity components of the dominant perturbation for $v_0/v_p = 0.2$, $n = 0.2$, $b = 0.02$ and $N_C = 200$. Normalization is done with respect to the amplitude of the radial velocity at the surface of the cylinder. Together, they show that the perturbation corresponds to a necking deformation. However, when v_0/v_p is increased to 5, the velocity components appear very different, as shown in Fig. 12b. At high extension speeds, the dominant perturbation appears to be localized to a region near the free surface. The perturbation looks like a surface instability, which would result in an undulating free surface; it does not look like a necking instability that would lead to multiple necking. The perturbations shown in Fig. 12b are similar to the surface instabilities in strained plastic solids which were studied by Hutchinson and Tvergaard (1980). They investigated the conditions under which the surface perturbations of a strained power law hardening plastic solid become unstable and they arrived at a critical strain condition involving the hardening exponent. In uniaxial tension, for $n = 0.1$, 0.2 and 0.3, the critical strain was 0.45, 0.56 and 0.66 respectively. From the type of data shown in Fig. 11, the saturation strain values for the same values of n are 0.55, 0.62 and 0.66. The close agreement in the critical strains between the two analyses suggests that the dominant perturbation at high extension speeds corresponds to a surface instability rather than a necking mode. By subjecting aluminum bars to a bend test, Hutchinson and Tvergaard observed the growth of micro-surface undulations into large ripples and they also found that micro-cracks developed along the troughs of these ripples and grew into shear fractures. Thus, it may be speculated that, as the neck-like perturbations are replaced by surface ripple-like perturbations beyond a critical extension speed, cracks could develop at the bottom of such ripples, leading to a fragmentation mechanism that is entirely different from the multiple necking mechanism. However, no experimental results are currently available to test the validity of this hypothesis. In the Grady and Benson (1983) experiments, the aspect ratio was approximately 0.01 and the highest value of v_0/v_p achieved was about 2.4, which is far below the critical value, as can be seen from Fig. 10.

5. Numerical analysis

By its very nature, perturbation analysis is concerned with the critical conditions for the onset of necking instabilities. It does not say much about the post-bifurcation evolution of the instability and its progress towards fragmentation. A numerical simulation of the Grady and Benson (1983) experiments has been conducted using the finite element analysis program ABAQUS in order to understand the fragmentation characteristics. One half of the extending cylinder has been modeled, from $Z = 0$ to $Z = L$. The cylinder has been modeled with eight noded linear brick elements with reduced integration. The finite element discretization had 398 elements along the length and 60 elements within the cross-section. At $Z = 0$, the cylinder was constrained in the axial direction and, at $Z = L$, the cylinder had an axial velocity $v_0 = \pi\dot{r}$, where $\dot{r}$ is the radial expansion speed in Grady and Benson (1983) experiment. The initial conditions were such that all points at a distance Z from the origin, had an axial velocity of $v_0 Z/L$. To account for the Poisson contraction, all material points also had an initial radial velocity of $-\nu v_0 R/L$ where ν is the Poisson's ratio. Following Sorensen and Freund (2000), the radius of the bar was given a small geometric imperfection of the form $R = A(1 - 2\xi\cos(\pi Z/L))$, in which the parameter ξ controls the magnitude of the imperfection. Calculations were carried out for either $\xi = 0$ or $\xi = 0.01$.

The material was modeled as an elastic—porous plastic material, whose yield function depends on the macroscopic Cauchy stress σ_{ij}, the matrix tensile flow stress σ_{m} and the current void volume fraction. The yield function can be represented as (Gurson, 1977; Tvergaard and Needleman, 1984),

$$\Phi(\sigma_{ij}, \sigma_{\mathrm{m}}, f) = \frac{\sigma_{\mathrm{e}}^2}{\sigma_{\mathrm{m}}^2} + 2f^* q_1 \cosh(3\sigma_{\mathrm{H}}/2\sigma_{\mathrm{m}}) - (1 + (q_1 f^*)^2) = 0 \tag{31}$$

where σ_{e} is the effective stress or Mises stress $(3/2\ S_{ij}\ S_{ij})^{1/2}$. S_{ij} is the deviatoric part of σ_{ij} and σ_{H} is the hydrostatic part of Cauchy stress, $\sigma_{kk}/3$. This model exhibits dilatational plasticity behavior as a result of the porosity. Tvergaard (1982) introduced the parameter q_1 with a value of 1.5 to obtain better agreement between the predictions of this model and the numerical studies of a periodic array of voids. Following Tvergaard and Needleman (1984), material failure by micro-void coalescence is modeled through the function f^* as follows.

$$\begin{aligned} &f^* = f, \quad f \leqslant f_{\mathrm{c}} \\ &f^* = f_{\mathrm{c}} + K(f - f_{\mathrm{c}}), \quad f > f_{\mathrm{c}} \end{aligned} \tag{32}$$

where $K = (1/q_1 - f_{\mathrm{c}})/(f_{\mathrm{F}} - f_{\mathrm{c}})$. Here f_{c} is the value of the void volume fraction at which void coalescence first occurs and f_{F} is its value at final failure. As f reaches f_{F}, f^* approaches $1/q_1$, at which stage the material loses its stress carrying ability. Thus, a failure criterion is directly built into the constitutive equations. An estimate of f_{c} obtained from a simple model is 0.15 (Brown and Embury, 1973) and a numerical study by Anderson (1977) suggests that f_{F} is approximately 0.25.

The void volume fraction is supposed to increase through the growth of existing voids and nucleation of new voids. The evolution law for void volume fraction is written as

$$\dot{f} = \dot{f}_{\mathrm{growth}} + \dot{f}_{\mathrm{nucleation}} \tag{33}$$

$$\dot{f}_{\mathrm{growth}} = (1 - f)\dot{\varepsilon}_{kk}^{\mathrm{p}} \tag{34}$$

$$\dot{f}_{\mathrm{nucleation}} = \frac{f_n}{s_n\sqrt{2\pi}} \exp\left[-\frac{1}{2}\left(\frac{\bar{\varepsilon}_{\mathrm{m}}^{\mathrm{p}} - \varepsilon_n}{s_n}\right)^2\right]\dot{\bar{\varepsilon}}_{\mathrm{m}}^{\mathrm{p}} \tag{35}$$

Here, $\dot{\varepsilon}_{ij}^{\mathrm{p}}$ is the plastic strain rate derived from the yield function given in Eq. (31) and $\bar{\varepsilon}_{\mathrm{m}}^{\mathrm{p}}$ is the matrix average plastic strain. It is related to the plastic train rate through

$$(1 - f)\sigma_y \dot{\bar{\varepsilon}}_{\mathrm{m}}^{\mathrm{p}} = \sigma_{ij}\dot{\varepsilon}_{ij}^{\mathrm{p}} \tag{36}$$

where σ_y is the tensile flow stress. The values of the constants appearing in these equations are $q_1 = 1.5$, $f_n = 0.01$, $s_n = 0.1$, $\varepsilon_n = 0.2$, $f_c = 0.15$, $f_F = 0.25$. The elastic modulus, the Poisson's ratio and the density of copper are 130 GPa, 0.3, 8930 kg/m^3, respectively and those of aluminum are 75 GPa, 0.35 and 2700 kg/m^3. The plastic strain–stress data for copper was taken from Nemat-Nasser and Li (1998) and that for aluminum was taken from Khan and Huang (1992).

6. Results of numerical analysis

Numerical simulations were conducted at a variety of extension speeds corresponding to radial expansion speeds of up to 250m/s. Some of the common features of the simulations are described using a typical case of a copper rod with $v_0 = 400$ m/s. As loading continues, when a critical strain is reached, plastic deformation becomes unstable and a large number of diffuse necks appear spontaneously along the length of the bar. This is seen in Figs. 13 and 14, which show the contour plots of the axial stress and the axial plastic strain, respectively. The contour plots show level curves of these quantities in the plane of average axial strain vs. the Z-coordinate. Since the overall strain increases with time, the abscissa can be viewed as time. At an imposed strain of about 0.34, uniform deformation gives way to multiple necking and further plastic deformation is mainly localized to the neck regions only. Porosity begins to develop inside the necked regions and its evolution is shown in Fig. 15. During the neck development phase, the individual necks interact with each other, leading to a situation where some of the necks cease to grow whereas the others continue to grow until the porosity reaches f_F, indicating fracture. In Fig. 15, six necks reach the final fracture stage. The strain beyond which the number of fragments remains constant is taken as the fracture strain. The development of porosity is accompanied by a complex evolution of stress state because of the decreased stress carrying ability of the necked regions. This can be seen in Fig. 13 where the axial stress drops rapidly as the bar undergoes fragmentation.

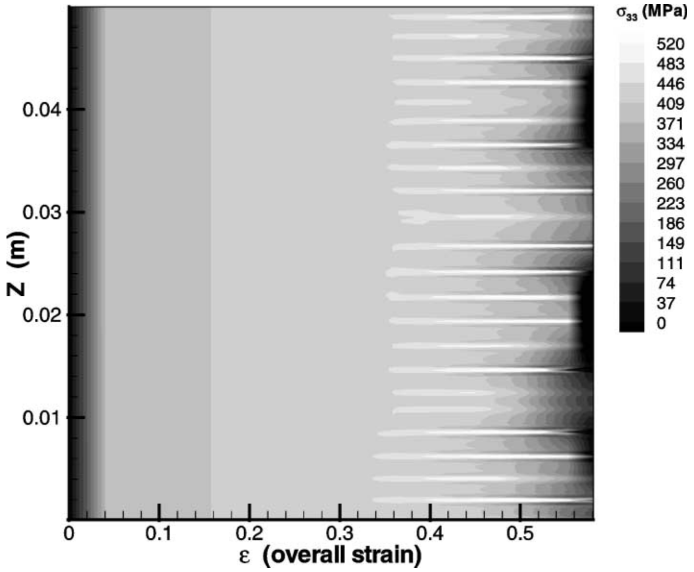

Fig. 13. Contour plots of the time evolution of axial stress along the length of the cylinder. The abscissa, which is the overall strain, represents the time. Spontaneous multiple necks appear all along the length of the cylinder at a critical strain.

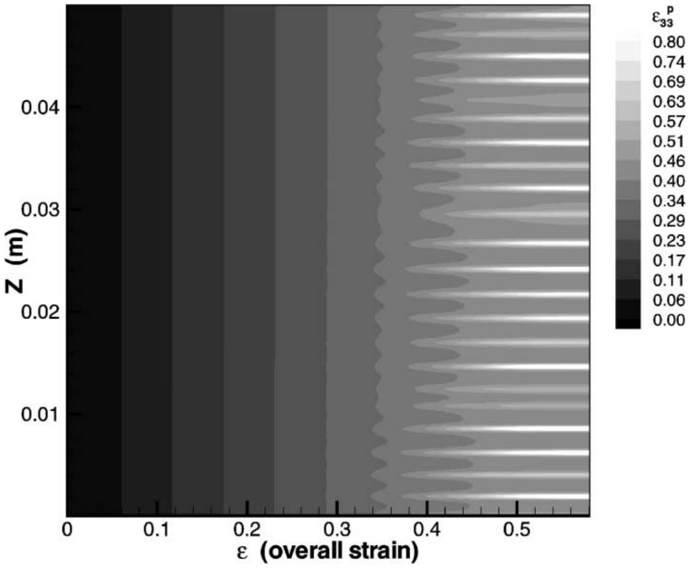

Fig. 14. Contour plots of the time evolution of axial plastic strain along the length of the cylinder. The abscissa, which is the overall strain, represents the time. Spontaneous multiple necks appear all along the length of the cylinder at a critical strain. These necks interact with each other and as a result, some of the necks arrest whereas the others continue to deform until fracture, leading to fragmentation.

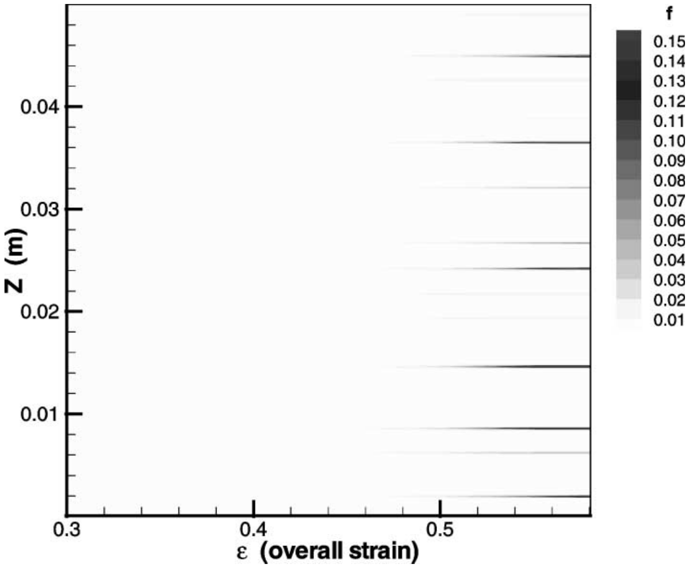

Fig. 15. Evolution of void volume fraction *f* inside the necked regions. Though porosity develops in many necks, only some of them reach the critical value to cause fracture.

Figs. 16–19 show the fragmentation results for copper and aluminum. A number of observations can be made. The size of the imperfection has no significant influence on the number of necks, number of fragments, bifurcation strain and the fracture strain. In fact, no imperfection is needed to simulate the

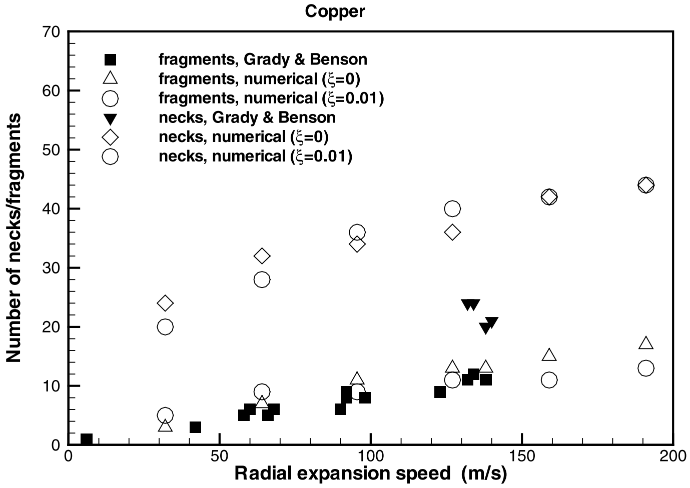

Fig. 16. A comparison between the numerical results and the experimental observations for copper. The simulations consistently overestimate the number of necks whereas excellent agreement is found for the number of fragments.

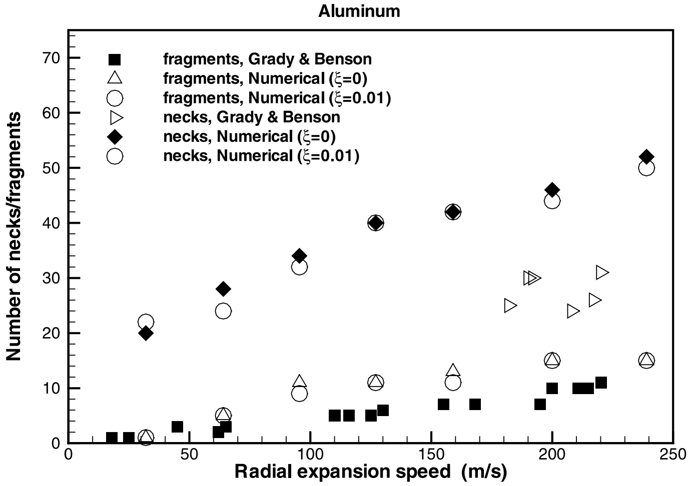

Fig. 17. A comparison between the numerical results and the experimental observations for aluminum. The simulations consistently overestimate the number of necks whereas good agreement is found for the number of fragments.

fragmentation behavior. The small round-off errors present in the nodal coordinates and the initial conditions are sufficient to cause the instability when the critical conditions are reached. Figs. 16 and 17 show that the numerical results consistently overestimate the number of necks as compared to the experimental values. One of the reasons for this difference could be the way the necks were counted in the experiments. Comparing Figs. 14 and 15, it can be seen that some of the necks arrest before developing any significant plastic deformation and the diameter of these arrested necks would not be significantly less than its neighborhood, thus contributing to their not being counted as arrested necks.

Very good agreement is seen between the numerical simulations and experimental results for the number of fragments for both materials. The simulations slightly overestimate the number of fragments for

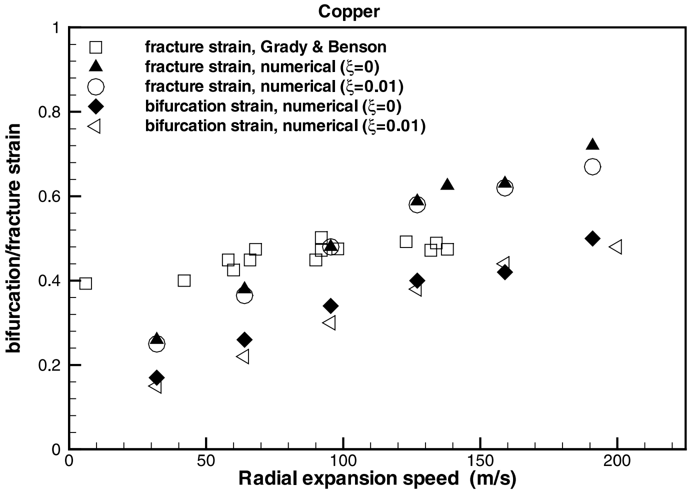

Fig. 18. A comparison between the numerical results and the experimental observations for copper. The numerical fracture strains closely approximate the experimental values.

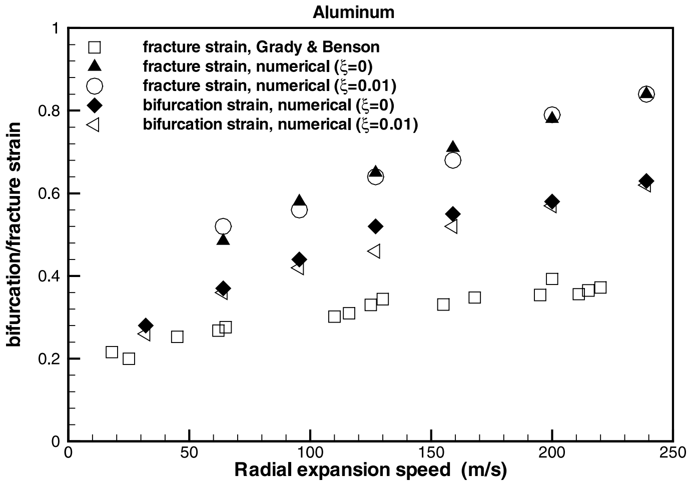

Fig. 19. A comparison between the numerical results and the experimental observations for aluminum. The numerical fracture strains overestimate the experimental values. This is possibly due to the uncertainty in the stress–strain relation at large strains. The shape of the stress–strain curve was seen to affect the bifurcation and fracture strains.

aluminum. The good agreement demonstrates that the numerical procedure used in this investigation can be used to predict the number of fragments in other cases also. From Figs. 18 and 19, there appears to be some discrepancy between the calculations and the experiments with respect to fracture strain. For copper, though the agreement is reasonable, the rate of increase of the fracture strain with expansion speed is not reproduced. However, the experimental fracture strain is consistently higher than the numerical bifurcation strain, as it should be. However, this is not so in case of aluminum. The reason for this could be the uncertainty in the constitutive data. As noted before, the bifurcation strain is a rather sensitive function of the exact shape of the stress–strain curve. Small differences in the shape of the curve have been observed to cause significant changes in the bifurcation strain. We believe that accurate constitutive characterization of the material up to large strains is necessary in order to accurately model the bifurcation and fracture strain.

Acknowledgements

The research support of the Office of Naval Research grant N00014-95-1-0239 and the Department of Energy, Office of Basic Engineering Sciences grant DE-FG02-95-ER14561 is gratefully acknowledged.

References

Altynova, M., Hu, X., Daehn, S., 1996. Increased ductility in high velocity electromagnetic ring expansion. Metallurgical and Materials Transactions 27A, 1837–1843.

Anderson, H., 1977. Analysis of a model for void growth and coalescence ahead of a moving crack tip. Journal of the Mechanics and Physics of Solids 25, 217–233.

Brown, L.M., Embury, J.D., 1973. The initiation and growth of voids at second phase particles. In: Microstructure and Design of Alloys, Cambridge.

Cheng, S.Y., Ariaratnam, S.T., Dubey, R.N., 1971. Axisymmetric bifurcation in an elastic–plastic cylinder under axial load and lateral hydrostatic pressure. Quarterly of Applied Mathematics 29, 41–51.

Follansbee, P.S., 1986. High-strain-rate deformation of FCC metals and alloys. In: Murr, L.E., Staudhammer, K.P., Meyers, M.A. (Eds.), Metallurgical applications of shock wave and high-strain-rate phenomena. M. Dekker, New York.

Fressengeas, C., Molinari, A., 1994. Fragmentation of rapidly stretching sheets. European Journal of mechanics A-Solid 13, 251–268.

Fyfe, I.M., Rajendran, A.M., 1980. Dynamic pre-strain and inertia effects on the fracture of metals. Journal of the Mechanics and Physics of Solids 28, 17–26.

Grady, D.E., Benson, D.A., 1983. Fragmentation of metal rings by electromagnetic loading. Experimental Mechanics 12, 393–400.

Gurson, A.L., 1977. Continuum theory of ductile rupture by void nucleation and growth. Part I. Yield criteria and flow rules for porous ductile media. Journal of Engineering Materials and Technology 99, 2–15.

Han, J.-B., Tvergaard, V., 1995. Effect of inertia on the necking behavior of ring specimens under rapid radial expansion. European Journal of Mechanics A-Solid 14, 287–307.

Hill, R., Hutchinson, J.W., 1975. Bifurcation phenomena in the plane tension test. Journal of the Mechanics and Physics of Solids 23, 239–264.

Hutchinson, J.W., Miles, J.P., 1974. Bifurcation analysis of the onset of necking in an elastic/plastic cylinder under uniaxial tension. Journal of the Mechanics and Physics of Solids 22, 61–71.

Hutchinson, J.W., Neale, K.W., 1977. Influence of strain-rate sensitivity on necking under uniaxial tension. Acta Metallugica 25, 839–846.

Hutchinson, J.W., Tvergaard, V., 1980. Surface instabilities on statically strained plastic solids. International Journal of Mechanical Sciences 22, 339–354.

Khan, A., Huang, S., 1992. Experimental and theoretical study of mechanical behavior of 1100 aluminum in the strain rate range 10^{-5}–10^4 s^{-1}. International Journal of Plasticity 8, 397–424.

Miles, J.P., 1971. Bifurcation in plastic flow under uniaxial tension. Journal of the Mechanics and Physics of Solids 19, 89–102.

Nemat-Nasser, S., Li, Y., 1998. Flow stress of FCC polycrystals with application to OFHC Cu. Acta Materialia 46, 565–577.

Pandolfi, A., Krysl, P., Ortiz, M., 1999. Finite element simulation of ring expansion and fragmentation: The capturing of length and time scales through cohesive models of fracture. International Journal of Fracture 95, 279–297.

Pao, Y.H., Gilat, A., 1989. Modeling 1100-O aluminum over a wide range of temperatures and strain rates. International Journal of Plasticity 5, 183–196.

Shenoy, V.B., Freund, L.B., 1999. Necking bifurcations during high strain rate extension. Journal of the Mechanics and Physics of Solids 47, 2209–2233.

Sorensen, N.J., Freund, L.B., 2000. Unstable neck formation in a ductile ring subjected to impulsive radial loading. International Journal of Solids and Structures 37, 2265–2283.

Storen, S., Rice, J.R., 1975. Localized necking in thin sheets. Journal of the Mechanics and Physics of Solids 23, 421–441.

Tvergaard, V., 1982. Influence of void nucleation on ductile shear fracture at a free surface. Journal of the Mechanics and Physics of Solids 30, 399–425.

Tvergaard, V., Needleman, A., 1984. Analysis of cup-cone fracture in a round tensile bar. Acta Metallurgica 32, 157–169.